SCIENCE ADVANCES | RESEARCH ARTICLE

MATERIALS SCIENCE

Spontaneous chemical functionalization via coordination of Au single atoms on monolayer MoS_2

He Liu[1]*, Daniel Grasseschi[2,3]*†, Akhil Dodda[4]*, Kazunori Fujisawa[5,6,7], David Olson[8], Ethan Kahn[9], Fu Zhang[9], Tianyi Zhang[9], Yu Lei[9], Ricardo Braga Nogueira Branco[10], Ana Laura Elías[6,7,11], Rodolfo Cruz Silva[5,12], Yin-Ting Yeh[6,7], Camila M. Maroneze[2], Leandro Seixas[2], Patrick Hopkins[8,13,14], Saptarshi Das[4,9], Christiano J. S. de Matos[2], Mauricio Terrones[1,6,7,9]†

Surface functionalization of metallic and semiconducting 2D transition metal dichalcogenides (TMDs) have mostly relied on physi- and chemi-sorption at defect sites, which can diminish the potential applications of the decorated 2D materials, as structural defects can have substantial drawbacks on the electronic and optoelectronic characteristics. Here, we demonstrate a spontaneous defect-free functionalization method consisting of attaching Au single atoms to monolayers of semiconducting MoS_2(1H) via S-Au-Cl coordination complexes. This strategy offers an effective and controllable approach for tuning the Fermi level and excitation spectra of MoS_2 via p-type doping and enhancing the thermal boundary conductance of monolayer MoS_2, thus promoting heat dissipation. The coordination-based method offers an effective and damage-free route of functionalizing TMDs and can be applied to other metals and used in single-atom catalysis, quantum information devices, optoelectronics, and enhanced sensing.

INTRODUCTION

Chemical surface functionalization has been used to tune the electronic, optical, and catalytic properties of two-dimensional (2D) transition metal dichalcogenides (TMDs) (*1*–*3*). Chemical functionalization commonly relies on the presence of lattice defects and physisorption methods to circumvent the chemical inertness of pristine semiconducting TMDs (*4*). Unfortunately, such routes inevitably modify the surface characteristics as well as the optical, thermal, and transport properties of the atomically thin layers (*5*–*9*). Most of the proposed MoS_2 functionalization routes are based on liquid exfoliated flakes, which have reduced and more reactive lateral sizes. In addition, this exfoliation route is not ideal for scaling up processes in the electronics and optoelectronics industries (*10*). For example, Voiry *et al.* (*6*) reported covalent functionalization using chemically exfoliated MoS_2, WS_2, and $MoSe_2$ with organohalides and its impact on their photoluminescence (PL) emission. Although this functionalization did not entirely rely on defect engineering, it is restricted to TMDs in the 1T phase, and the exfoliation procedure involves harsh chemical treatments, such as butyllithium. Efforts have also been made to functionalize chemical vapor deposition (CVD)–grown TMDs. For example, Ding *et al.* (*2*) reported that thiol functionalization of CVD-grown MoS_2 led to an increase in the PL intensity due to the passivation of S vacancies by the ligand, thus relying on the presence of inherent defects to achieve functionalization. However, in this case, the thiol does not provide perfect healing to the crystalline structure; thus, the charge mobility of a pristine crystal is not reestablished/recovered. To the best of our knowledge, chemically bonding single atoms, molecules, or clusters to the surface of pristine crystalline TMD monolayers remains a challenge. For metal monochalcogenides, Lei *et al.* (*11*) proposed the formation of coordination complexes on the surface InSe and showed that the presence of nonbonding electron pairs can be exploited by applying Lewis acid-base concepts to form coordination bonds with metal ions. As a result, the electronic properties of InSe were tailored and p-type doping was observed through this functionalization approach.

In this work, we developed a route to functionalize monolayers of MoS_2 with individual Au atoms via the formation of S-Au-Cl coordination complexes ($[Au(MoS_2)Cl_x]$) on the TMD surface. The $[Au(MoS_2)Cl_x]$ coordination complexes have been synthesized by taking advantage of the lone pair electrons of the S atoms present in the MoS_2 lattice. Unlike substitutional doping or defect passivation, the formation of the metal-MoS_2 coordination complexes does not rely on the presence of additional defects on the 1H-MoS_2 but induces significant changes in the optical, thermal, and electrical properties. Density functional theory (DFT) calculations confirmed that single $AuCl_x$ complex would bond to S atoms, rather than randomly absorbed on top of Mo atoms or over the vacant spots of the hexagonal lattice, and scanning transmission electron microscopy (STEM) imaging revealed the presence of Au single atoms fixed on top of S atoms. During the Au functionalization, the Au^{3+} precursor was spontaneously reduced to Au^{1+} on the TMD surface before forming the Au─S coordination bonds. This Au─S bond results in an efficient transfer of electrons from the MoS_2 valence band with high contribution of S 3p orbitals to the Au 5d and 6s orbitals, thus tuning the Fermi level of MoS_2 monolayers. By treating MoS_2 with

---

[1]Department of Chemistry, The Pennsylvania State University, University Park, PA 16802, USA. [2]MackGraphe—Graphene and Nanomaterials Research Center, Mackenzie Presbyterian University, 01302-907 São Paulo, Brazil. [3]Surface Chemistry and Nanomaterials Laboratory, Inorganic Chemistry Department, Chemistry Institute, Federal University of Rio de Janeiro (UFRJ), 21941-909 Rio de Janeiro, Brazil. [4]Engineering Science and Mechanics, The Pennsylvania State University, University Park, PA 16802, USA. [5]Research Initiative for Supra-Materials (RISM), Shinshu University, 4-17-1 Wakasato, Nagano 380-8553, Japan. [6]Department of Physics, The Pennsylvania State University, University Park, PA 16802, USA. [7]Center for 2-Dimensional and Layered Materials, The Pennsylvania State University, University Park, PA 16802, USA. [8]Department of Mechanical and Aerospace Engineering, University of Virginia, Charlottesville, VA 22904, USA. [9]Department of Materials Science and Engineering, The Pennsylvania State University, University Park, PA 16802, USA. [10]Department of Aerospace Engineering, The Pennsylvania State University, University Park, PA 16802, USA. [11]Department of Physics, Binghamton University, Binghamton, NY 13902, USA. [12]Global Aqua Innovation Center, Faculty of Engineering, Shinshu University, 4-17-1 Wakasato, Nagano 8553, Japan. [13]Department of Materials Science and Engineering, University of Virginia, Charlottesville, VA 22904, USA. [14]Department of Physics, University of Virginia, Charlottesville, VA 22904, USA.
*These authors contributed equally to this work.
†Corresponding author. Email: mut11@psu.edu (M.T.); dgrasseschi@iq.ufrj.br (D.G.)

different Au concentrations, we found an effective way to tune the Fermi level of MoS_2 via controlled p-type doping, as measured in field-effect transistors (FETs). In addition, Au functionalization leads to high exciton-to-trion ratios in the PL spectra of monolayer MoS_2. The stability of the S-Au-Cl coordination sphere leads to the existence of $[Au(MoS_2)Cl_x]$ complexes that results in a major enhancement on the thermal boundary conductance across MoS_2 monolayers. This coordination method could also be used to synthesize Ag single atoms on MoS_2. The isolation and anchorage of single noble atoms via a solution-phase chemical approach pave the way for large-scale manipulation of single atoms, leading to high-performance catalysis and quantum information applications (*12*).

RESULTS

Synthesis of $[Au(MoS_2)Cl_x]$ complexes: Single Au atoms in motion

MoS_2 monolayers were synthesized by CVD on Si/SiO_2 substrates using powder precursors (see Materials and Methods for details). Optical microscopy, Raman spectroscopy, and PL spectroscopy were carried out to characterize the MoS_2 flakes (see fig. S1). The coordination reaction between the MoS_2 monolayers with $HAuCl_4$ was performed by dipping the as-grown MoS_2 into an ethanol solution of $HAuCl_4$ exhibiting various concentrations for 10 min, following washing and drying. High-resolution STEM (HR-STEM) imaging using a high-angle annular dark-field (ADF) detector was conducted to study the atomic structure of the Au atoms on MoS_2. The ADF intensity changes, depending on the *Z*-number of atoms ($\sim Z^{1.6-1.9}$) (*13*); thus, the higher *Z*-number Au atoms stand out in the MoS_2 lattice. As shown in Fig. 1A, bright single Au atoms on top of the MoS_2 lattice can be observed. These Au atoms remain isolated, rather than aggregated. The largest Au aggregate found by STEM is shown in the inset of Fig. 1A, where four Au atoms occupy neighboring S sites. Note that we consider this as a planar aggregate of Au single atoms, rather than a regular Au cluster, as the atomic spacing corresponds to that of the S in the MoS_2 lattice in a planar view, rather than the predicted 1.34 Å interatomic distance between Au atoms in planar clusters (*14*, *15*). Atomic resolution STEM-ADF images confirmed the presence of Au single atoms and their preferred position on the MoS_2 monolayer, which is directly on top of the S sites [see Fig. 1 (A and B)]. The DFT-simulated STEM-ADF image (Fig. 1C) was obtained on the basis of the model shown in Fig. 1A (inset) and exhibits an excellent agreement with the experimental image. Single-atom Ag could also be synthesized via $AgNO_3$ ethanol solution displaying similar Ag-MoS_2 structures (see fig. S2). An ADF intensity line scan was also performed across the single Au atom shown in Fig. 1 (B and C) (vertical gray line in the figures). In the experimentally acquired ADF intensity line profile (Fig. 1D), besides observing the ADF intensity peak at the Mo site and 2S sites, an intense peak corresponding to the Au-2S site was found matching the simulated ADF intensity at the Au-2S site (Fig. 1E and fig. S3).We believe that Cl atoms are bonded to the Au single ions to complete the Au coordination sphere and balance the charge on the Au atoms in the form of $[Au(MoS_2)Cl]$ and $[Au(MoS_2)Cl_3]$ complexes (see below for details). However, STEM simulations conducted for $[Au(MoS_2)]$, $[Au(MoS_2)Cl]$, and $[Au(MoS_2)Cl_3]$ structures (fig. S3) indicate the absence of Cl atoms on our experimental STEM images. We believe that this is due to the electron beam (e-beam) irradiation at 80 keV that may be displacing Cl atoms during imaging. HR-STEM was also used to observe changes in the position of individual Au atoms on the MoS_2 surface over time. Figure 1F shows selected frames of a video (see movie S1) showing the movement of a single Au atom on MoS_2 under e-beam irradiation. The beam provides energy to the Au atom, leading to a dynamic atom displacement. It can be observed that the Au atom is capable of hopping from one S coordination site to another. A clear trajectory (gray curve) was determined for the atom movement. For the first 100 s of the referred video, the tracked Au atom stayed directly above the same S atom, and it then jumped toward a neighboring S site, occupying that for several more seconds. The displacement distance of each hop is shown in Fig. 1G. The Au atom moves to the nearest S atom most of the time but can cover a distance of 2 nm during one frame (10 s per frame). The displacement distance covered by the Au atom shows that the atom stays almost static when it is on top of S, while it moves much more actively when it is on top of Mo. We could not find a Au atom that would stay above the Mo atom or at any position other than above a S site for several seconds; thus, we conclude that those positions are only transitory and not stable configurations. This observation indicates that stronger interactions between the Au and S atoms make S sites energetically favorable. The movement of single Au atoms, if deterministically manipulated, could be further exploited in future quantum information devices (*12*).

$[Au(MoS_2)Cl_x]$ complex coordination sphere

To further understand the chemical nature of the functionalization and to characterize the Au oxidation state, x-ray photoelectron spectroscopy (XPS) was carried out. Figure 2A shows the Au 4f core-level spectrum of the $[Au(MoS_2)Cl_x]$ complex (green curve). The spectrum can be well fitted by two sets of doublet peaks (red and blue curves) that can be assigned to Au^{3+}, from the $HAuCl_4$ precursor, and Au^{1+}, indicating spontaneous Au reduction on MoS_2. Specifically, the Au^{3+} signature corresponds to the $4f_{5/2}$ ($4f_{7/2}$) peak at 91.0 (87.4) eV, while the Au^{1+} signature relates to the $4f_{5/2}$ ($4f_{7/2}$) peak at 88.2 (84.5) eV, which are comparable to other studies reporting Au ions with S-containing ligands (*16*, *17*). Huang *et al.* (*18*) have reported that gold can be spontaneously reduced from Au^{3+} to Au^0 nanoparticles in a solution of chemically exfoliated MoS_2. In this work, we demonstrate that Au^{3+} can be reduced into Au^{1+} in the form of single atoms due to the formation of a coordination bond to the nondefective surface of CVD-grown MoS_2 monolayers. On the basis of the standard reduction potentials for the Au^{3+}/Au^{1+} pair (0.926 V) and MoS_2 (−0.090 V), electrons from the MoS_2 monolayer can be donated to Au^{3+} so that Au^{3+} is reduced to Au^{1+} (*19*). In addition, according to Pearson, in hard-soft acid and base theory (*20*, *21*), soft ligands, such as S, stabilize linear Au^{1+} complexes (*22*).

The formation of Au—S bonds was also confirmed by the S 2p core-level spectra shown in Fig. 2B. In pristine MoS_2 monolayers, the S shows a doublet peak corresponding to a $2p_{1/2}$ peak at 163.0 eV and a $2p_{3/2}$ peak at 161.9 eV. After functionalization, the doublet peak shifted to a higher binding energy (0.8 eV shift), thus confirming the formation of Au—S bonds. The donation of lone pair electrons from S to Au atoms results in a higher electrostatic attraction on the inner shells of S, causing XPS peaks with higher binding energy (*17*). The shift further confirms the formation of Au—S bonds. Therefore, the formation of Au^{1+}—S bonds contributes to the stabilization, partial reduction, and formation of single Au ions on the MoS_2 surface. In addition, the absence of water inhibits the Au^{1+}

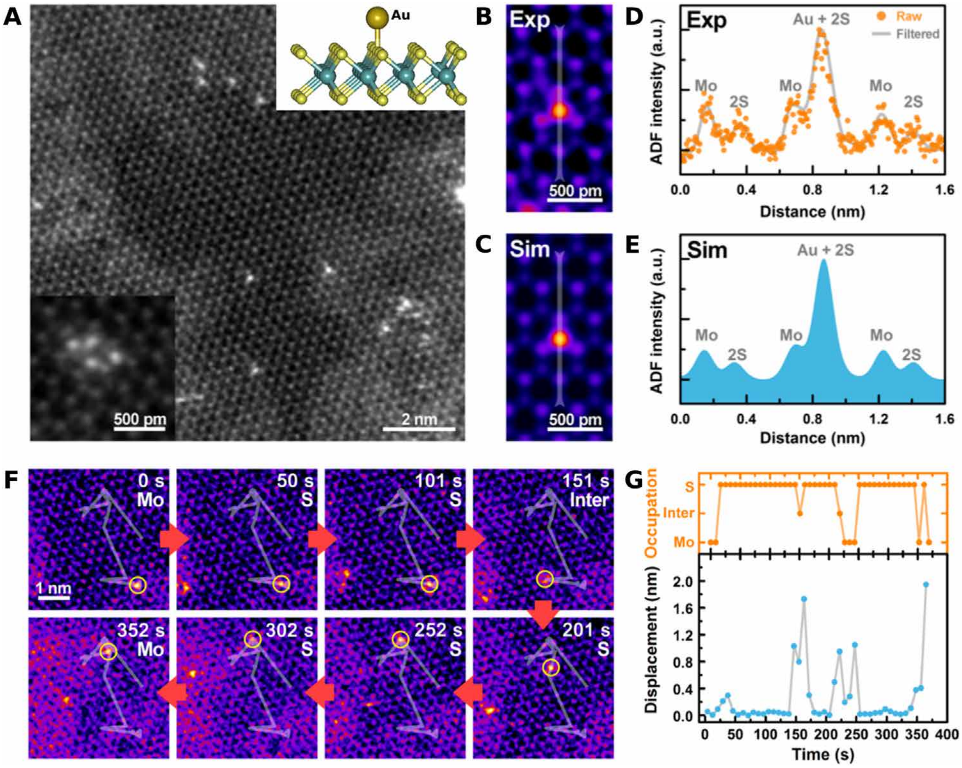

Fig. 1. Synthesis of Au single atoms on monolayer MoS$_2$ flakes. (**A**) HR-STEM images of [Au(MoS$_2$)Cl$_x$] featuring the single Au atoms on S sites. Insets: The structure model of Au-MoS$_2$ used for STEM image simulation (top right) and the higher-magnification STEM image of a Au aggregate found on MoS$_2$ (bottom left).(**B** and **D**) High-angle ADF (HAADF) images and *Z*-contrast line scan [along the vertical gray line in (B)] of one Au single atom on MoS$_2$, revealing the position of the Au atom to be directly on top of the S atom. a.u., arbitrary units. (**C** and **E**) TEM simulation of one Au atom directly on top of one S atom in MoS$_2$ lattice and *Z*-contrast line scan of the simulation image. The simulated TEM image and line scan match exactly with experimental data, confirming the atomic structure of Au single atoms directly bonded on S atoms on the MoS$_2$ surface. (**F**) Time-lapse images of Au single atoms on MoS$_2$. The Au single atoms can move on the MoS$_2$ plane under the e-beam irradiation during STEM characterization. The full video can be viewed in the Supplementary Materials. The gray curves show the trail of one Au atom moving on MoS$_2$. (**G**) The statistical analysis of the position of one Au atom and displacement distance between each movement.

disproportionation reaction that results in the formation of Au^0 and Au^{3+}, which, in turn, prevents the formation of gold clusters or nanoparticles (*22*). In addition, XPS data reveal the presence of Cl with a Au:Cl ratio of 1:3, as shown in fig. S5, which could be due to the presence of unreacted Au precursor HAuCl$_4$ and/or from AuCl$_x$ complexes coordinated on MoS$_2$ surface (see Discussion). Similar peak shifting of S 2p orbitals and additional peak splitting were observed for Ag-MoS$_2$ functionalizations demonstrating the formation of Ag—S bonds (see fig. S4) (*23*).

To understand the effect of the single AuCl$_x$ complex functionalization on the optical properties of monolayer MoS$_2$, we carried out PL spectroscopy measurements. As seen in Fig. 2C, PL studies reveal the presence of a pristine MoS$_2$ monolayer characteristic signature, due to its direct band gap at the *K*(*K*′) point. The peak shown in Fig. 2C can be deconvoluted, via fitting with two Lorentzians, into a neutral exciton (X; red) at 1.83 eV and a negative trion (X$^-$; blue) located at 1.79 eV. It can also be seen that the X$^-$ trion was markedly quenched, while the neutral exciton X intensity was enhanced after the Au functionalization. The formation of the coordination bonds between the S and Au atoms results in MoS$_2$ electrons being transferred to the Au atoms, thus leading to a decrease in the X$^-$ trion intensity and an increase in the neutral exciton intensity in MoS$_2$ (*3*). Therefore, we believe that the recorded changes in the PL after functionalization are caused by the p-type doping of MoS$_2$ via AuCl$_x$ coordination. The p-type doping level of MoS$_2$ via AuCl$_x$ coordination can be carefully controlled by exposing the MoS$_2$ monolayers to different concentrations of HAuCl$_4$ solutions. Figure 2D shows the exciton-to-trion intensity ratio as a function of the Au concentration. It can be clearly seen that this ratio increases with the Au concentration, offering an effective approach to sharpen the PL spectra of MoS$_2$. A more detailed discussion on the p-type doping effect is available below (Fig. 3). Raman spectra of monolayer MoS$_2$ before and after the Au functionalization exhibit the characteristic in-plane E′ and out-of-plane A′$_1$ modes, without noticeable frequency nor intensity differences (fig. S1). As shown in table S1, no significant changes can be observed either in the Mo—S bond lengths and the Mo—S—Mo bond angles, for the optimized Au coordination in the 1H phase MoS$_2$.

The formation of the Au—S bond was further investigated by DFT calculations, which were performed to identify the most energy-favorable structure for the [Au(MoS$_2$)Cl$_x$] complex [shown in Fig. 3 (A and B)]. Cl atoms were added to the Au coordination sphere to balance the charge on the Au atoms and complete its coordination sphere, which is also confirmed by XPS (fig.S5). Thus, three different structures were evaluated, with an isolated Au atom ([Au(MoS$_2$)]), with one Cl atom ([Au(MoS$_2$)Cl]), and with three Cl atoms ([Au(MoS$_2$)Cl$_3$]). After the optimization simulations, three available coordination sites, known as the H (hollow), Mo, and 2S

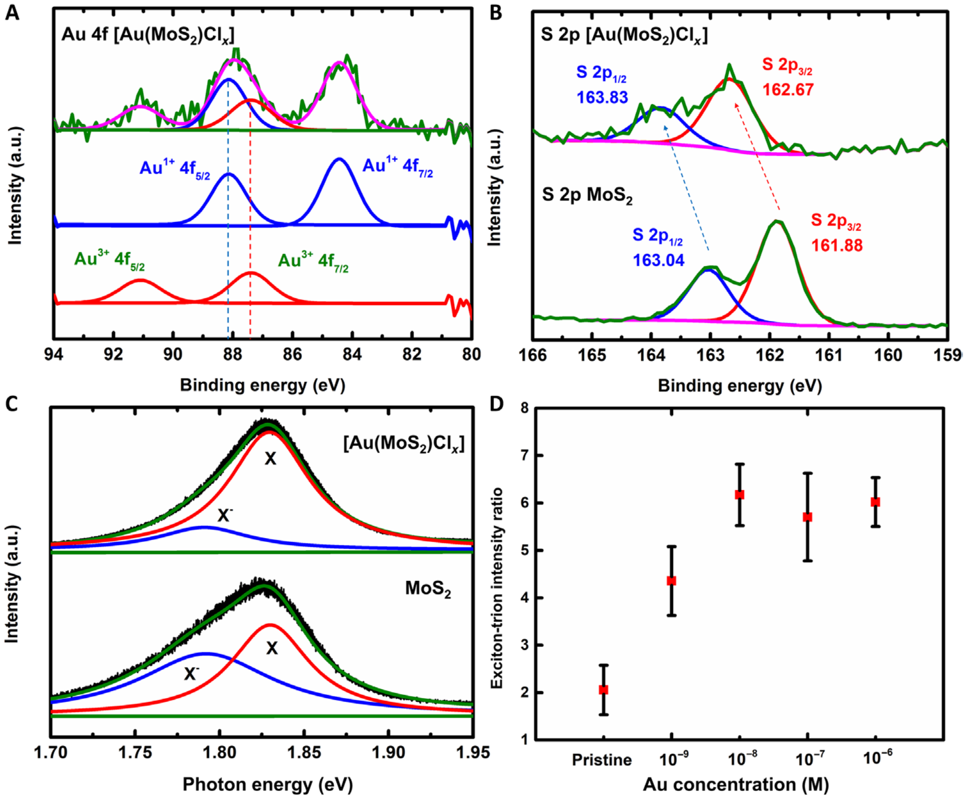

Fig. 2. Spectroscopic studies of the [Au(MoS$_2$)Cl$_x$] complex. (**A**) XPS spectra of Au 4f orbit on Au-MoS$_2$. The green curve is the original spectrum after C$_{1s}$(248.8 eV) calibration. The blue and red curves are fittings of the original data, which show the presence of Au^{3+} and Au^{1+}. We believe that the presence of Au^{3+}comes from the unreacted HAuCl$_4$ precursor, whereas the Au^{1+} from the reduction reaction with MoS$_2$. The purple curve is the sum of the blue and red curves. (**B**) S 2p orbit of pristine and Au functionalized MoS$_2$. The green curve is the original spectrum after C$_{1s}$(248.8 eV) calibration. The blue and red curves are fittings that show the S 2p$_{1/2}$ and 2p$_{3/2}$ peaks, respectively. The S 2p orbitals shift to higher energy because of the loss of outer electrons to Au—S bonds. (**C**) PL spectrum of pristine and functionalized MoS$_2$ monolayers. The A exciton is deconvoluted into the trion (X$^-$) (blue curve) and exciton (X) (red curve) peaks through Lorentzian functions. After doping, the trion intensity decreased, while the exciton intensity increased, which corresponds well with the p-type doping effect of the Au^{1+}. (**D**) Exciton-to-trion intensity ratio of pristine and functionalized MoS$_2$ with different precursor Au concentrations.

sites, were identified. In the H site, the Au is located at the center of the hexagon formed by the lattice projection on a plane (fig. S6); in the Mo site, the Au sits on top of one Mo atom and is bound to the three adjacent S atoms. Last, the 2S site, where the Au atom is positioned on top of a S atom, was found to be the most stable site by an energy difference of 550 meV (Fig. 3, A and B). Illustration of the H and S sites of Ag-MoS$_2$ complexes can be found in fig. S7 and table S1, where the S site is found to be the most favorable for Ag single atoms. These results are in good agreement with the HR-STEM images depicted in Figs 1B and 2A and fig. S2, where Au and Ag locate preferentially over S atoms. Furthermore, to understand the spontaneous reduction of single AuCl$_x$ complexes, the charge distribution of the three systems was calculated and analyzed using the Voronoi deformation density method. The Au atom charge in the [Au(MoS$_2$)Cl$_3$] and [Au(MoS$_2$)Cl] optimized geometries were found to be +0.80 and 0.40 eV, respectively, indicating that the charge transfer from the S atoms leads to the spontaneous reduction of Au^{3+} to Au^{1+} during the Au—S bond formation. The [Au(MoS$_2$)Cl$_3$] projected charge transfer map shown in Fig. 3B indicates a higher electron concentration in the atoms near the Au—S bond. On the contrary, the MoS$_2$ regions far from the AuCl$_3$ exhibited a higher hole concentration, which can be understood as p-type of doping. For the [Au(MoS$_2$)Cl], the projected charge transfer map shown in fig. S8 indicates a very small hole concentration on MoS$_2$, whereas for Au-MoS$_2$, we found a high electron concentration on the MoS$_2$ and an n-type of doping, showing Cl atoms bound to Au to provide the p-type doping observed experimentally. The [Au(MoS$_2$)Cl] and [Au(MoS$_2$)Cl$_3$] data are in good agreement with XPS, where the Au 4f core-level spectra confirm the Au^{1+} formation and the Cl 2p spectra indicate the presence of Cl on the surface. In addition, the exciton-to-trion intensity ratio changes observed in the PL spectra (Fig. 2, C and D) show a clear p-type doping of MoS$_2$.

From the calculated electronic band structure, displayed in Fig. 3C, we notice that the MoS$_2$ remained a direct gap semiconductor after functionalization. However, the bands near the Fermi level were drastically affected by the presence of single Au^{1+} ions coordinated on the MoS$_2$ monolayer, with the corresponding wave functions overlapping with Au orbitals. A localized state is also apparent in the functionalized structure above the Fermi level corresponding to Au d orbitals. The mentioned changes in the band structure are expected to affect the optical properties of MoS$_2$. In this context, optical absorbance measurements conducted in MoS$_2$, before and after functionalization, provide some valuable information that can be correlated to band structure. Figure 3D depicts the average spectra of 10 pristine (black) and [Au(MoS$_2$)Cl$_x$] (pink) samples; some of the individual spectra can be found in fig. S9. After Au coordination,

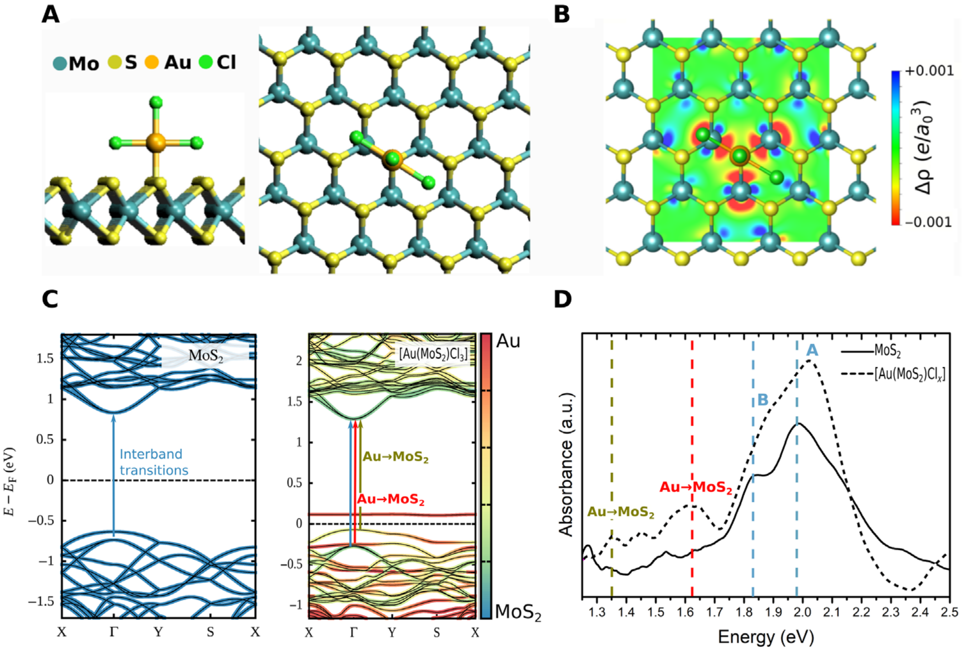

Fig. 3. Band structure studies of the [Au(MoS$_2$)Cl$_x$] complex. (**A**) DFT-optimized structure for the [Au(MoS$_2$)Cl$_3$] complex. Chlorine atoms were considered to complete the Au coordination sphere. (**B**) Charge transfer map of the [Au(MoS$_2$)Cl$_3$] complex showing a higher hole concentration along most of the MoS$_2$ sheet (blue surface), and a pronounced electron concentration on the Mo and S atoms near the Au atom (red surface), commensurate with a p-type doping effect of the Au^{1+}. (**C**) Electronic band structure of pristine MoS$_2$ and of the [Au(MoS$_2$)Cl$_3$] complex, both calculated without considering the spin-orbit coupling. Electronic transitions are indicated by vertical arrows. In the [Au(MoS$_2$)Cl$_3$] complex, besides the pristine MoS$_2$ excitons A and B, charge transfer transitions are expected between the MoS$_2$ state (blue line) and the Au localized states (red line). (**D**) Room temperature absorbance spectra of the [Au(MoS$_2$)Cl$_x$] complex (dotted line) and of pristine MoS$_2$ (black). A slight blue shift of the A and B excitons and new features associated with charge transfer transitions at energies lower than 1.7 eV are observed, as expected from the electronic band structure of the [Au(MoS$_2$)Cl$_3$] complex shown in (C).

there is a small blue shift in the A (1.83 to 1.88 eV) and B (1.98 to 2.02 eV) exciton absorption peaks, as predicted by the DFT calculations (blue arrow in Fig. 3C). The Tauc plots and its representative fitting of absorption edge show that the MoS$_2$ preserved a direct gap after the functionalization (fig. S10) (*24*). In addition, a new broad absorption band located at a low energy, between 1.5 and 1.7 eV, can be observed in the Au-MoS$_2$ absorption spectra, which can be assigned to charge transfer transitions from localized states in the Au ions to the conduction band, with major contributions from MoS$_2$ electronic states (red arrow in Fig. 3C). Another charge transfer transition can be seen at 1.35 eV, which can be assigned to an electronic transition from states on the valence band showing a mixture of Au and MoS$_2$ to the conduction band (green) arrow in Fig. 3C. It is worth mentioning that the band structure calculated for [Au(MoS$_2$)Cl] (fig. S11) could also explain the electronic transitions observed experimentally. Since both [Au(MoS$_2$)Cl] and [Au(MoS$_2$)Cl$_3$] lead to p-type doping, both complexes could be well formed during the functionalization process; however, the [Au(MoS$_2$)Cl$_3$] has a better fit with the experimental data because of the higher binding energy and p-type doping induced on MoS$_2$.

Fermi level tuning through AuCl$_x$ coordination

To further investigate the influence of AuCl$_x$ complex coordination on the electronic properties of monolayer MoS$_2$, we designed and fabricated back-gated FETs (BGFETs) (fig. S12) Figure 4A shows the schematic of the monolayer MoS$_2$ BGFET. Figure 4 (B and C) indicates the transfer characteristics, i.e., drain current (I_{DS}) versus back-gate voltage (V_{BG}) and output characteristics, i.e., drain current (I_{DS}) versus drain bias (V_{DS}), respectively, of a representative pristine MoS$_2$ BGFET. The field-effect mobility (μ_{FE}) extracted from the peak transconductance was found to be ~25 cm^2/V·s, which is comparable to the mobility values reported for exfoliated single-crystal material (*25*). This confirms the superior quality of the as-grown monolayer MoS$_2$. The ON state current, which is proportional to the μ_{FE} and the charge in the channel, i.e., C_{OX}*($V_{BG} - V_T$), where V_T is the threshold voltage of the device and C_{OX} is the oxide capacitance, was found to be ~120 μA/μm at V_{DS} = 8 V and V_{BG} = 10 V, further confirming the high performance of the monolayer MoS$_2$ BGFET. The subthreshold slope (SS) of the device was found to be 350 mV per decade, which indicates a reasonably clean interface with the back gate despite the wet transfer process carried out on the MoS$_2$ during device fabrication. Figure 4D shows device-to-device variations in pristine MoS$_2$ BGFETs. These same devices were then treated with ethanol solution with various concentration of HAuCl$_4$ such as 10^{-10}, 10^{-9}, and 10^{-6} M. Figure 4 (E to G) display the transfer characteristics at V_{DS} = 1 V for 10 representative devices after functionalization. Note that MoS$_2$ BGFETs were treated with the lowest concentration of HAuCl$_4$ at first (Fig. 4E), measured, and then subsequently treated with increasing concentrations (Fig. 4, F and G). For higher HAuCl$_4$ concentrations, the threshold voltage becomes increasingly positive, i.e., it shifts toward the right, indicating that the Au coordination acts as a p-dopant. From TEM, XPS, and DFT results, we can then infer that the AuCl$_x$ complexes coordinate to the S atoms, forming a fixed charge on the channel,

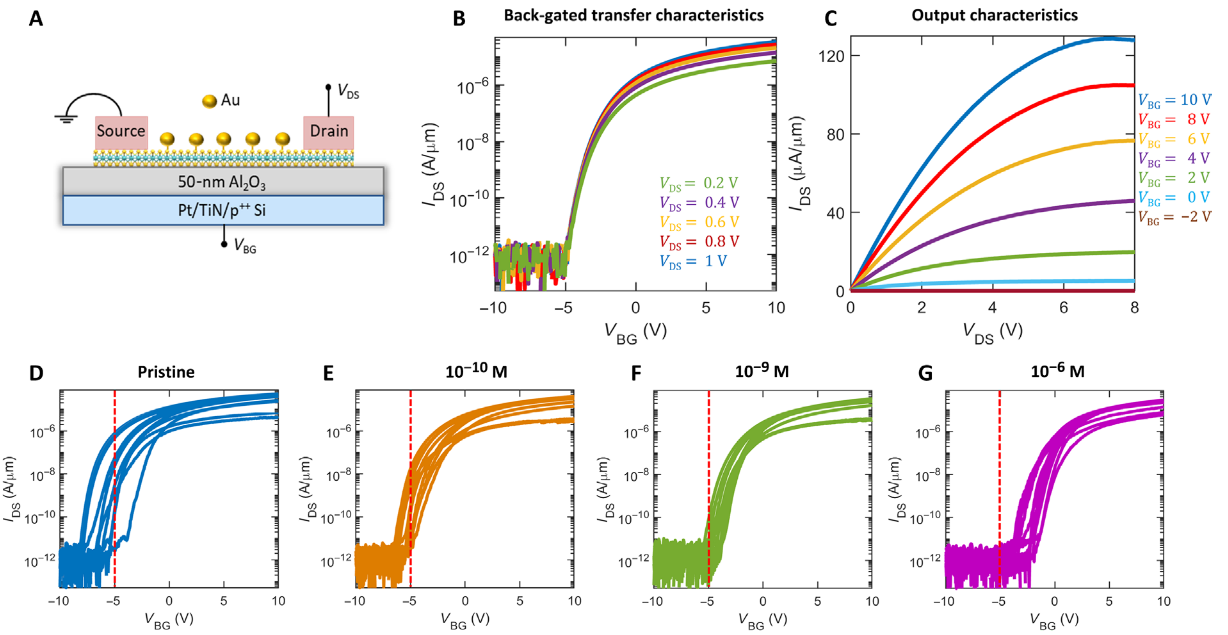

Fig. 4. Fermi level tuning using gold doping. (**A**) Schematic of a BGFET involving coordination of gold on the MoS_2 channel. (**B**) Back-gated transfer characteristics of the MoS_2 FET. (**C**) Output characteristics of the MoS_2 FET. (**D** to **G**) Drain current (I_{DS}) versus back-gate voltage (V_{BG}) characteristics with a drain bias of 1 V. (D) Pristine, (E) 10^{-10} M, (F) 10^{-9} M, and (G) 10^{-6} M concentrations of $HAuCl_4$ in ethanol.

which influences the threshold voltage, based on the equation given below

$$\Delta V_T = \frac{\Delta Q_F}{c_{ox}} \tag{1}$$

Here, ΔV_T corresponds to the change in threshold voltage, while ΔQ_F is the change in the fixed charge. As the fixed charge on the semiconducting material changes, the flat band voltage increases, meaning that the Fermi level moves closer to the valence band. Table 1 shows the statistics for threshold voltage, SS, and field-effect mobilities for 10 representative devices corresponding to different concentrations of $HAuCl_4$. The threshold voltage shift in the devices is extracted for the electron branch using the iso-current method for a current value of 100 nA/μm for $V_D = 1$ V. As the concentration of $HAuCl_4$ increases, the coordination of $AuCl_x$ complexes to the S also increases, which leads to an increased fixed charge on the channel and, ultimately, a shift in the threshold voltage. Figure S13A shows the error bar plot of threshold voltage variations for different doping concentrations. Mobility values and SS from the statistics suggest that neither the ON-state nor the OFF-state device performance are significantly degraded because of the Au doping. It is also observed that mobility and SS values remain almost constant throughout for various Au concentrations. On the basis of the threshold voltage shift, we further computed the number of $AuCl_x$ complexes coordinated to the MoS_2 monolayer using the equation below

$$n = \frac{c_{ox} \Delta V_T}{q} \tag{2}$$

Here, q is the electronic charge. Figure S13B shows the error bar plot of the number of coordinated $AuCl_x$ complexes versus concentration for an area of 10 nm by 10 nm. Note that this particular area was chosen to compare the number of Au atoms coordinated to S through Eq. 2 and then compared with the number obtained from HR-STEM. The results obtained for the 10^{-6} M concentration (ca. eight single complexes per 100 nm^2) match perfectly with the number of Au atoms coordinated to S shown in the HR-STEM image in Fig. 1B.

The stability of the single $AuCl_x$ complex functionalization is further confirmed via FET measurements carried out 1 year after the functionalization process (fig. S15). It was observed that the devices did not degrade over time, ensuring the devices and the functionalization method to be highly reliable. Therefore, we can conclude that our Au functionalization technique clearly results in a precise tuning of the Fermi level positions by adjusting the $HAuCl_4$ solution concentration.

Thermal boundary conductance measurements

To further understand the effects of the single $AuCl_x$ complex functionalization of MoS_2, we carried out thermal boundary conductance measurements via time-domain thermoreflectance (TDTR). Previous measurements via frequency-domain thermoreflectance have demonstrated that the thermal conductance at graphene contacts can be extracted via a multi-modulation frequency approach (*26*). Recently, Brown *et al.* (*27*) have shown that thermal conductance values at the metal/$MoSe_2$ interfaces can be extracted via a TDTR mapping technique. To capture the appropriate conductance at the Al/MoS_2/SiO_2 interface (see Materials and Methods), we have used the magnitude of the thermoreflectance signal to locate single crystals of MoS_2 and subsequently performed full TDTR measurements near the center of the crystals. Figure 5A depicts a representative micrograph where the thermoreflectance overall magnitude was used to find a MoS_2 single crystal. The uniformity of the thermoreflectance magnitude in this region suggests that the thermal conductance across the interface is relatively uniform. The TDTR curve and best fit for the conductance, h_K, are presented in Fig. 5B for the pristine MoS_2 monolayer, with the inset showing the early picosecond acoustic response used to extract the thickness of the Al layer (*28*, *29*). A summary

Table 1. Threshold voltage, SS, mobility, and ON/OFF ratio statistics of the 10 representative devices for various concentrations of $HAuCl_4$.

Gold coordination (M)	Threshold voltage V_T (V)	Subthreshold slope (SS) (mV/decade)	Mobility [μ_{FE} (cm^2/V·s)]	ON/OFF ratio
Pristine	−4.4 ± 2.5	360 ± 150	15 ± 10	10^6–10^7
10^{-10}	−3.0 ± 1.0	370 ± 150	15 ± 5	10^6–10^7
10^{-9}	−2.0 ± 0.8	340 ± 140	15 ± 5	10^6–10^7
10^{-6}	−0.42 ± 1.0	325 ± 150	15 ± 5	10^6–10^7

of the h_K results obtained for $AuCl_x$ functionalized MoS_2 monolayers at various metal concentrations is presented in Fig. 5C.

In general, we observed that the thermal conductance at the Al/MoS_2/SiO_2 interfaces is commensurate with the Au concentration. In this context, chemical functionalization of graphene via oxygen plasma treatment has been previously reported to increase the conductance by 50 and 100% at these interfaces when Au and Al are chosen as the metal contact, respectively (*30*, *31*). As in these works, we attribute the enhanced conductance at the Al/MoS_2/SiO_2 interface to the enhanced reactivity of the MoS_2 caused by chemical functionalization. As Al is required to be in contact with some fraction of Au ions, the reasons for the enhanced conductance could be attributed to the additional pathway of conduction via the electronic system or through an improvement of the bonding state at the Al/MoS_2 interfacial region through functionalization. In addition, functionalization of MoS_2 monolayers will inherently change the localized vibrational density of states, thus offering additional pathways of conduction. Various reports have previously examined the thermal conductance at the MoS_2/SiO_2 interfaces via Raman spectroscopy (*32*, *33*). There, a conductance value of ~15 MW m^{-2} K^{-1} was extracted, which is similar to those presented here. However, a direct comparison between the two approaches is not possible, as the conductance at the Al/MoS_2/SiO_2 interface is inherently measured in our experiment, whereas just the MoS_2/SiO_2 interface without a metal topcoat is measured in the referred studies (*30*, *31*). The major enhancement on the thermal boundary conductance of monolayer MoS_2, obtained upon Au functionalization, can be applied to increase the heat dissipation rate in vertically stacked 2D transistors.

DISCUSSION

The formation of chemical bonds is crucial for an effective and nondestructive functionalization of 2D TMD materials. In this work, we demonstrated the formation of the [$Au(MoS_2)Cl_x$] complex, which results in the transfer of electrons from MoS_2 valence band formed by Mo 4d and S 3p orbitals into the Au valence orbitals (6s and 5d), as indicated by the high mixing of Mo, S, and Au states on the bands near the Fermi level shown in Fig. 3. In the STEM images shown in Fig. 1, we observe that the distribution of Au single atoms is fixed on top of S sites rather than randomly dispersed. The movie (Supplementary Materials) and trajectory image (Fig. 1G) further confirm that Au atoms prefer to sit on S sites even when moving. The displacement distance analysis also concludes that the Au atoms stay static on S and move immediately to adjacent S when found on top of Mo. These pieces of evidence confirm that the Au atoms have a much higher affinity toward S atoms, indicating chemical interactions between Au and S atoms. STEM simulations conducted for [$Au(MoS_2)$], [$Au(MoS_2)Cl$], and [$Au(MoS_2)Cl_3$] structures (fig. S3) indicate the absence of Cl atoms in our experimental STEM images. It is due to the e-beam irradiation at 80 keV, which might have displaced Cl atoms before image acquisition. The [$Au(MoS_2)Cl_x$] complex is further studied via XPS. The shift of S 2p spectra (Fig. 2B) that indicate electron transfer from S to Au agrees with the formation of a covalent bond through Au coordination with S atoms, where MoS_2 acts as ligands donating electrons to Au atoms. XPS data for the Au and Cl core level depicted in fig. S5 show the presence of Cl atoms on the [$Au(MoS_2)Cl_x$] sample with a Au:Cl ratio of 1:3. We constructed three different structures with isolated Au ion, Au with one Cl, and Au with three Cl on MoS_2 via DFT calculations. For [$Au(MoS_2)Cl$] and [$Au(MoS_2)Cl_3$] complexes, the electrons are transferred from the MoS_2 to Au, promoting the Au reduction and a p-type doping on the MoS_2, thus matching our experimental observations. In contrast, for [$Au(MoS_2)$], electrons are transferred from Au atoms to MoS_2, leading to n-type doping. When considering 3Cl as additional ligand, the Au—S binding energy (−1.4 eV) is higher than the Au—S binding energy (−0.86 eV) without Cl, which could facilitate the formation of single $AuCl_x$ complexes and prevent aggregation. Thus, the simulations indicate the need of Cl ligands to complete gold's coordination sphere and balance the charges.

The Au 4f spectrum also reveals two states of Au present on the MoS_2 surface, namely, Au^{1+} and Au^{3+}. We believe that the presence of Au^{3+} comes from the unreacted $HAuCl_4$ precursor, while the Au^{1+} comes from the reduction with MoS_2. The standard reduction potential difference between the Au^{3+}/Au^{1+} pair ($AuCl_4^-$/$AuCl_2^-$ = 0.926 V) and MoS_2 (−0.090 V) causes the spontaneous reduction of Au^{3+} to Au^{1+} by MoS_2. In addition and according to Pearson hard-soft acid and base theory, the reduction from Au^{3+} to Au^{1+} makes Au atoms softer, thus promoting a strong bonding to S with a more covalent character since S atoms are soft ligands known to stabilize linear Au^{1+} complexes. Because of the filled 3p S orbitals, MoS_2 acts as a pi-donor ligand. This way, when Au^{1+} ion forms coordination bonds with MoS_2, the Au redox potential should decrease considerably, preventing further reduction into its elemental state. For example, $[Au(SCN)_2]^-$ complexes have a redox potential of +0.66 V, whereas $[AuCl_2]^-$ complexes have a much higher redox potential (E_0 = +1.15 V), as shown in fig. S14. The absence of elemental Au atoms also prevents the formation of Au clusters and particles since both Au^{3+} and Au^{1+} are positively charged ions that show electrostatic repulsion. The repulsion and coordination bonding thus resulted in the stable Au single ions that we see in Fig. 1.

Furthermore, we believe that this coordination-based functionalization strategy is general and could be applied to other metals and TMD systems. Many transition metals such as Fe, Ni, and Pt have empty d orbitals that have been well known for forming coordination complexes with S-based ligands (*34*–*36*). Since S is considered a soft base in Pearson hard-soft acid and base theory, we would

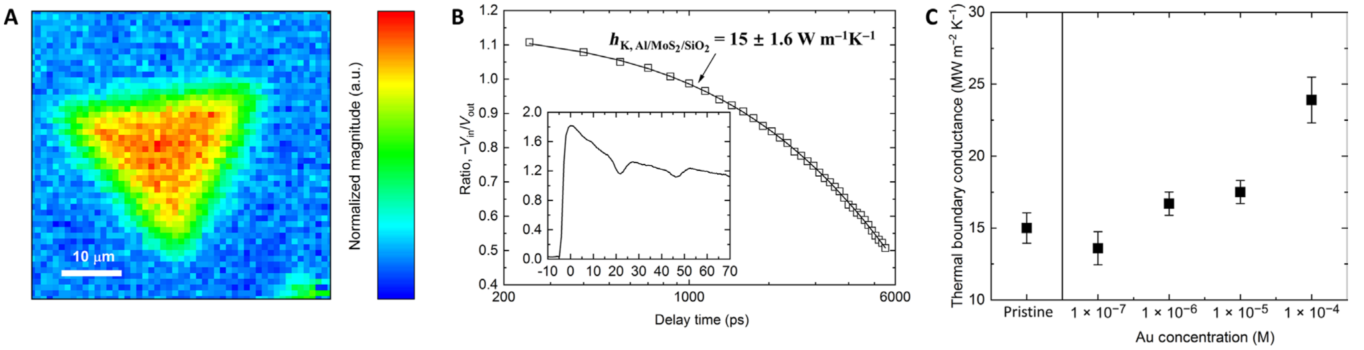

Fig. 5. Thermal conductance enhancement from single AuCl$_x$ complexes. (**A**) TDTR magnitude mapping of a pristine single-crystal MoS_2 flake. (**B**) TDTR model and best fit for the conductance at the Al/pristine MoS_2/SiO_2 interface. The inset shows the picosecond acoustics response at earlier time delays. (**C**) Results for the thermal boundary conductance at Al/Au-MoS_2/SiO_2 interfaces.

expect soft atoms such as Pt and Ni to form stronger coordination bonds when compared to Fe and Ti. The coordination sphere will also depend on the ligands from the precursors. In addition, since Se and Te are even softer than S, we believe that the interaction between Au and Ag with selenides or tellurides would be stronger. The controlled doping of Se and Te into MoS_2 systems may offer a way to control the location of Au single atoms since Au—Se bonds should be more favorable (*37*).

In this work, we successfully prepared [Au(MoS_2)Cl_x] and Ag-MoS_2 coordination complexes where Au and Ag single atoms were bonded to S atoms via coordination bonds. This approach does not rely on defects, such as vacancies, in the MoS_2 crystalline layers but does have a significant impact on the optical, electrical, and thermal properties of the functionalized monolayer MoS_2. The formation of the coordination complex [Au(MoS_2)Cl_x] led to the transfer of electrons from MoS_2 to the noble metal, which introduced p-type doping to the functionalized atomically thin semiconductor. Moreover, the degree of p-type doping can be fine-tuned by varying the Au precursor ($HAuCl_4$) concentrations, thus controlling the Fermi level of MoS_2 and the exciton-to-trion relative population. Furthermore, the MoS_2 surface functionalization with single noble metal atoms creates midgap states in the electronic structure of MoS_2 and yields band displacements near the Fermi level, which effectively modified the absorbance spectra in the visible range and are responsible for shifts in the PL excitonic emissions. The single noble metal atom functionalization has resulted in a major enhancement of the thermal boundary conductance across monolayer MoS_2 interfaces, which could be applied to increase the heat dissipation rate of vertically stacked 2D transistors based on this and other semiconducting TMDs. In addition, the synthesis of single atoms introduced in this work could also be exploited in other applications such as single-atom catalysis, quantum information devices, optoelectronics, and enhanced sensing.

MATERIALS AND METHODS

Synthesis of monolayer MoS_2

Monolayer MoS_2 was synthesized by a salt-assisted CVD method, similar to previous publications (*38*, *39*). NaBr (Alfa Aesar, 99%) was ground into a fine powder with a mortar and pestle and then mixed with MoO_2 in a 10:1 ratio by weight. For growth of monolayer films, 2 mg of the salt/oxide mixture was placed at the bottom of a ceramic boat and a piece of SiO_2 (300 nm)/Si substrate was placed facing down over the mixture, with ca. 2 mm of space between the mixture and substrate. Sulfur powder (100 mg; Alfa Aesar, 95%, 300 mesh) was used as the sulfur source. The growth substrate was placed at the center of a 1-inch-diameter horizontal tube furnace (Lindberg/Blue M), while the sulfur powder was placed upstream outside of the furnace and 30 cm away from the growth substrates. Before the synthesis experiments, the tube was flushed with 400 standard cubic centimeter per minute (sccm) of Ar for 20 min, and then, the flow was reduced to 100 sccm. The furnace was then heated to 800°C for 20 min and then held for 5 min. The sulfur powder was separately heated to 220°C for 5 min and held for 5 min, while the furnace was kept at 800°C.

Synthesis of the [Au(MoS_2)Cl_x] complex

The functionalization was performed by dipping the Si/SiO_2 substrate with the CVD MoS_2 into an ethanol solution of $HAuCl_4$ with concentrations between 1×10^{-2} to 1×10^{-9} M for 10 min. The functionalized [Au(MoS_2)Cl_x] sample was then immersed in isopropanol (IPA) for a few seconds to remove excess $HAuCl_4$, followed by N_2 drying. Last, the sample was kept in vacuum for 10 min before the measurements. To exclude the effect of ethanol or IPA adsorption on the flake surface, pristine samples were also washed with ethanol and IPA, dried with N_2, and kept in vacuum for 10 min.

Scanning transmission electron microscopy

STEM imaging was carried out in a FEI Titan^3 G2 60/300 operated at 80 kV to reduce irradiation damage. A high-angle ADF (HAADF) detector was used to collect ADF signal. A Gaussian blur filter was applied using the ImageJ software to reduce the noise and enhance the visibility of the detailed structure, but raw images were used for acquiring the line profile of the ADF intensity. STEM-ADF image simulations were conducted using the QSTEM package. Simulation parameters such as acceleration voltage, spherical aberration (C_3 and C_5), convergence angle, and inner/outer angle for the HAADF detector were set according to experimental conditions. Note that before the TEM imaging, the CVD-grown MoS_2 was first transferred to a TEM grid and then functionalized by 1×10^{-6} M $HAuCl_4$ in ethanol solution.

Device fabrication

BGFETs were fabricated using a 50-nm alumina (Al_2O_3) film as the gate oxide and a stack of Pt/TiN/p^{++}Si as the back gate electrode.

First, CVD-grown MoS_2 was transferred onto the alumina sample; then, the sample was spin coated with A6 polymethyl methacrylate (PMMA), followed by e-beam lithography to specify the 2-μm channels and then separating them out by sulfur hexafluoride (SF_6) etch under 5°C for 30 s. After each step, the sample was rinsed in acetone for 30 min, followed by a rinse in IPA. To define the source and drain contacts, the sample was then spin coated with methyl methacrylate, followed by A3 PMMA. Using e-beam lithography, source and drain contacts were then patterned and further developed by using 1:1 mixture of 4-methyl-2-pentanone and IPA for 60 s. Forty nanometers of Ni and 30 nm of Au were deposited onto the patterns using e-beam evaporation. Lift-off of the evaporated materials was carried out by immersing the sample in acetone for 30 min, followed by an IPA final rinse.

Electrical characterization

Electrical characterization of the fabricated devices and coordinated devices was performed in a Lake Shore CRX-VF probe station under high vacuum condition using a Keysight B1500A parameter analyzer.

Thermal boundary conductance measurements

A nominal 80-nm Al film was deposited on specimens via e-beam evaporation to serve as the metal transducer in our experiment. The 808.5-nm wavelength beam of a 80-MHz Ti:sapphire oscillator was spectrally separated into pump and probe paths. The pump path was amplitude-modulated via an electro-optic modulator at 8.4 MHz, creating a frequency-dependent heating event at the surface of the Al-coated MoS_2. The probe was mechanically delayed in time and monitored the thermoreflectance at the sample surface due to the pump-induced heating event. With a 10× objective, the $1/e^2$ diameters of the pump and probe were 14 and 11 μm, respectively. We fitted the data to the radially symmetric heat diffusion equation for the conductance, h_K, of the $Al/MoS_2/SiO_2$ interfaces and the thermal conductivity of the underlying thermal oxide. Additional information regarding the specific analyses of TDTR can be found elsewhere (*40–42*). Single-crystal MoS_2 flakes were located by mounting our samples on a two-axis stage, which was oriented to minimize changes in the pump/probe radii over the measurement range.

XPS measurements

XPS measurements were conducted in a high-resolution Thermo Scientific XPS with monochromatic Al Kα x-ray source. The binding energies were calibrated with C_{1s} binding energy of 284.8 eV. The analysis of peak fitting was performed on XPSPEAK41 software.

Optical absorbance measurements

Optical absorption measurements were performed using a home-made setup. For excitation, a supercontinuum white light source (NKT Photonics), ranging from 400 to 2400 nm, was coupled to an optical fiber with core diameter of 9 μm and the output was collimated using a 5× Newport objective [0.10 numerical aperture (NA)]. The beam was then reflected using a Thorlabs visible non-polarizing cube beam splitter (400 to 700 nm) to a Nikon TU Plan Fluor EPI 50× objective (0.8 NA), which focused the beam on the sample at normal incidence. The reflected signal was collected and collimated by the same 50× objective. After transmission through the cube beam splitter, the beam was focused onto the input of a Thorlabs multimode fiber with core diameter of 500 μm using a 10× Newport objective (0.25 NA), connected to a Yokogawa Optical Spectrum Analyzer operation in the 350- to 1700-nm range. In this setup, the position where the spot was focused on the sample was determined by directing the reflected beam to a Thorlabs USB charge-coupled device camera (1024 × 768 resolution) on which an image was formed using a Thorlabs infinity-corrected lens (focus, 200 mm). For imaging, another visible beam splitter was placed before the camera lens and a diffused white light light-emitting diode source was used to illuminate the sample. To obtain absorbance spectra, the bare substrate was used as a reference.

First-principles calculations

Density functional calculations were performed using the SIESTA code (*43*) with a DZP localized basis set, energy shift of 0.03 eV, and mesh cutoff of 400 rydberg. The exchange-correlation functional was described by the gradient generalized approximation with a Perdew-Burke-Ernzerhof parameterization (*44*). We used a 4 × 4 diagonal supercell for the electronic band structure and 3 × 2 orthorhombic supercells for real-space charge density plots. Brillouin zone sampling was based on Γ-centered Monkhorst-Pack method with 4 × 4 grid for supercells (*45*). A vacuum spacing of 20 Å was added to avoid interaction among periodic layers. Structural optimization was performed with a force tolerance of 0.010 eV/Å.

SUPPLEMENTARY MATERIALS

Supplementary material for this article is available at http://advances.sciencemag.org/cgi/content/full/6/49/eabc9308/DC1

REFERENCES AND NOTES

1. S. S. Chou, M. De, J. Kim, S. Byun, C. Dykstra, J. Yu, J. Huang, V. P. Dravid, Ligand conjugation of chemically exfoliated MoS_2. *J. Am. Chem. Soc.* **135**, 4584–4587 (2013).
2. Q. Ding, K. J. Czech, Y. Zhao, J. Zhai, R. J. Hamers, J. C. Wright, S. Jin, Basal-plane ligand functionalization on semiconducting 2H-MoS_2 monolayers. *ACS Appl. Mater. Interfaces* **9**, 12734–12742 (2017).
3. S. Mouri, Y. Miyauchi, K. Matsuda, Tunable photoluminescence of monolayer MoS_2 via chemical doping. *Nano Lett.* **13**, 5944–5948 (2013).
4. M. Chhowalla, H. S. Shin, G. Eda, L.-J. Li, K. P. Loh, H. Zhang, The chemistry of two-dimensional layered transition metal dichalcogenide nanosheets. *Nat. Chem.* **5**, 263–275 (2013).
5. C. Backes, N. C. Berner, X. Chen, P. Lafargue, P. LaPlace, M. Freeley, G. S. Duesberg, J. N. Coleman, A. R. McDonald, Functionalization of liquid-exfoliated two-dimensional 2H-MoS_2. *Angew. Chem. Int. Ed. Engl.* **54**, 2638–2642 (2015).
6. D. Voiry, A. Goswami, R. Kappera, C. de Carvalho Castro e Silva, D. Kaplan, T. Fujita, M. Chen, T. Asefa, M. Chhowalla, Covalent functionalization of monolayered transition metal dichalcogenides by phase engineering. *Nat. Chem.* **7**, 45–49 (2015).
7. K. Y. Ko, J.-G. Song, Y. Kim, T. Choi, S. Shin, C. W. Lee, K. Lee, J. Koo, H. Lee, J. Kim, T. Lee, J. Park, H. Kim, Improvement of gas-sensing performance of large-area tungsten disulfide nanosheets by surface functionalization. *ACS Nano* **10**, 9287–9296 (2016).
8. M. Amani, D.-H. Lien, D. Kiriya, J. Xiao, A. Azcatl, J. Noh, S. R. Madhvapathy, R. Addou, K. C. Santosh, M. Dubey, K. Cho, R. M. Wallace, S.-C. Lee, J.-H. He, J. W. Ager III, X. Zhang, E. Yablonovitch, A. Javey, Near-unity photoluminescence quantum yield in MoS_2. *Science* **350**, 1065–1068 (2015).
9. J. Suh, T.-E. Park, D.-Y. Lin, D. Fu, J. Park, H. J. Jung, Y. Chen, C. Ko, C. Jang, Y. Sun, R. Sinclair, J. Chang, S. Tongay, J. Wu, Doping against the native propensity of MoS_2: Degenerate hole doping by cation substitution. *Nano Lett.* **14**, 6976–6982 (2014).
10. S. Presolski, M. Pumera, Covalent functionalization of MoS_2. *Mater. Today* **19**, 140–145 (2016).
11. S. Lei, X. Wang, B. Li, J. Kang, Y. He, A. George, L. Ge, Y. Gong, P. Dong, Z. Jin, G. Brunetto, W. Chen, Z.-T. Lin, R. Baines, D. S. Galvão, J. Lou, E. Barrera, K. Banerjee, R. Vajtai, P. Ajayan, Surface functionalization of two-dimensional metal chalcogenides by Lewis acid–base chemistry. *Nat. Nanotechnol.* **11**, 465–471 (2016).
12. J. T. Muhonen, J. P. Dehollain, A. Laucht, F. E. Hudson, R. Kalra, T. Sekiguchi, K. M. Itoh, D. N. Jamieson, J. C. McCallum, A. S. Dzurak, A. Morello, Storing quantum information for 30 seconds in a nanoelectronic device. *Nat. Nanotechnol.* **9**, 986–991 (2014).
13. P. Hartel, H. Rose, C. Dinges, Conditions and reasons for incoherent imaging in STEM. *Ultramicroscopy* **63**, 93–114 (1996).
14. E. M. Fernández, J. M. Soler, L. C. Balbás, Planar and cagelike structures of gold clusters: Density-functional pseudopotential calculations. *Phys. Rev. B* **73**, 235433 (2006).

15. J. P. Perdew, Energetics of charged metallic particles: From atom to bulk solid. *Phys. Rev. B* **37**, 6175 (1988).
16. Y. Xue, X. Li, H. Li, W. Zhang, Quantifying thiol–gold interactions towards the efficient strength control. *Nat. Commun.* **5**, 4348 (2014).
17. H. Kitagawa, N. Kojima, T. Nakajima, Studies of mixed-valence states in three-dimensional halogen-bridged gold compounds, $Cs_2Au^{I}Au^{III}X_6$, (X = Cl, Br or I). Part 2. X-Ray photoelectron spectroscopic study. *J. Chem. Soc. Dalt. Trans.* , 3121–3125 (1991).
18. X. Huang, Z. Zeng, S. Bao, M. Wang, X. Qi, Z. Fan, H. Zhang, Solution-phase epitaxial growth of noble metal nanostructures on dispersible single-layer molybdenum disulfide nanosheets. *Nat. Commun.* **4**, 1444 (2013).
19. S. Lu, C. Li, Y. F. Zhao, Y. Y. Gong, L. Y. Niu, X. J. Liu, Tunable redox potential of nonmetal doped monolayer MoS_2: First principle calculations. *Appl. Surf. Sci.* **384**, 360–367 (2016).
20. R. G. Pearson, Hard and soft acids and bases. *J. Am. Chem. Soc.* **85**, 3533–3539 (1963).
21. G. Klopman, Chemical reactivity and the concept of charge- and frontier-controlled reactions. *J. Am. Chem. Soc.* **90**, 223–234 (1968).
22. J. Reedijk, K. R. Poeppelmeier, *Comprehensive Inorganic Chemistry II* (Elsevier, ed. 2, 2013).
23. J. F. Moulder, W. F. Stickle, P. E. Sobol, K. D. Bomben, Handbook of X-ray photoelectron spectroscopy: A reference book of standard spectra for identification and interpretation of XPS data, in *Surface and Interface Analysis*, J. Chastain, Ed. (Perkin-Elmer Corporation, ed. 1, 1992).
24. P. Y. Yu, M. Cardona, *Fundamentals of Semiconductors* (Springer, 1999).
25. D. S. Schulman, A. J. Arnold, S. Das, Contact engineering for 2D materials and devices. *Chem. Soc. Rev.* **47**, 3037–3058 (2018).
26. J. Yang, E. Ziade, C. Maragliano, R. Crowder, X. Wang, M. Stefancich, M. Chiesa, A. K. Swan, A. J. Schmidt, Thermal conductance imaging of graphene contacts. *J. Appl. Phys.* **116**, 023515 (2014).
27. D. B. Brown, W. Shen, X. Li, K. Xiao, D. B. Geohegan, S. Kumar, Spatial mapping of thermal boundary conductance at metal–molybdenum diselenide interfaces. *ACS Appl. Mater. Interfaces.* **11**, 14418–14426 (2019).
28. C. Thomsen, H. J. Maris, J. Tauc, Picosecond acoustics as a non-destructive tool for the characterization of very thin films. *Thin Solid Films* **154**, 217–223 (1987).
29. G. T. Hohensee, W.-P. Hsieh, M. D. Losego, D. G. Cahill, Interpreting picosecond acoustics in the case of low interface stiffness. *Rev. Sci. Instrum.* **83**, 114902 (2012).
30. P. E. Hopkins, M. Baraket, E. V. Barnat, T. E. Beechem, S. P. Kearney, J. C. Duda, J. T. Robinson, S. G. Walton, Manipulating thermal conductance at metal-graphene contacts via chemical functionalization. *Nano Lett.* **12**, 590–595 (2012).
31. B. M. Foley, S. C. Hernández, J. C. Duda, J. T. Robinson, S. G. Walton, P. E. Hopkins, Modifying surface energy of graphene via plasma-based chemical functionalization to tune thermal and electrical transport at metal interfaces. *Nano Lett.* **15**, 4876–4882 (2015).
32. E. Yalon, Ö. B. Aslan, K. K. H. Smithe, C. J. McClellan, S. V. Suryavanshi, F. Xiong, A. Sood, C. M. Neumann, X. Xu, K. E. Goodson, T. F. Heinz, E. Pop, Temperature-dependent thermal boundary conductance of monolayer MoS_2 by raman thermometry. *ACS Appl. Mater. Interfaces* **9**, 43013–43020 (2017).
33. E. Yalon, C. J. McClellan, K. K. H. Smithe, M. Muñoz Rojo, R. L. Xu, S. V. Suryavanshi, A. J. Gabourie, C. M. Neumann, F. Xiong, A. B. Farimani, E. Pop, Energy dissipation in monolayer MoS_2 electronics. *Nano Lett.* **17**, 3429–3433 (2017).
34. D. Selimann, M. Geck, M. Moll, Transition-metal complexes with sulfur ligands. 62. Hydrogen evolution upon reaction of protons with sulfur-coordinated iron(II) complexes. Investigation of the proton, hydrogen and hydride interactions with iron 1,2-benzenedithiolate complexes. *J. Am. Chem. Soc.* **113**, 5259–5264 (1991).
35. D. Sellmann, D. Häussinger, F. Knoch, M. Moll, Transition metal complexes with sulfur ligands. 117.[1] A reaction cycle for nickel mediated thioester formation from alkyl, CO, and thiolate groups modeling the acetyl-coenzyme A synthase function of CO dehydrogenase. *J. Am. Chem. Soc.* **118**, 5368–5374 (1996).
36. B. V. Petrovic, M. I. Djuran, Z. D. Bugarcic, Binding of platinum(II) to some biologicaly important thiols. *Met. Based. Drugs.* **6**, 355–360 (1999).
37. C. T. Le, D. J. Clark, F. Ullah, J. I. Jang, V. Senthilkumar, Y. Sim, M. J. Seong, K.-H. Chung, J. W. Kim, S. Park, S. H. Rhim, G. Kim, Y. S. Kim, Impact of selenium doping on resonant second-harmonic generation in monolayer MoS_2. *ACS Photonics.* **4**, 38–44 (2017).
38. S. Li, S. Wang, D.-M. Tang, W. Zhao, H. Xu, L. Chu, Y. Bando, D. Golberg, G. Eda, Halide-assisted atmospheric pressure growth of large WSe_2 and WS_2 monolayer crystals. *Appl. Mater. Today* **1**, 60–66 (2015).
39. H. Kim, D. Ovchinnikov, D. Deiana, D. Unuchek, A. Kis, Suppressing nucleation in metal–organic chemical vapor deposition of MoS_2 monolayers by alkali metal halides. *Nano Lett.* **17**, 5056–5063 (2017).
40. D. G. Cahill, Analysis of heat flow in layered structures for time-domain thermoreflectance. *Rev. Sci. Instrum.* **75**, 5119–5122 (2004).
41. A. J. Schmidt, X. Chen, G. Chen, Pulse accumulation, radial heat conduction, and anisotropic thermal conductivity in pump-probe transient thermoreflectance. *Rev. Sci. Instrum.* **79**, 114902 (2008).
42. P. E. Hopkins, J. R. Serrano, L. M. Phinney, S. P. Kearney, T. W. Grasser, C. T. Harris, Criteria for cross-plane dominated thermal transport in multilayer thin film systems during modulated laser heating. *J. Heat Transfer* **132**, 81302 (2010).
43. J. M. Soler, E. Artacho, J. D. Gale, A. García, J. Junquera, P. Ordejón, D. Sánchez-Portal, The SIESTA method for *ab initio* order- *N* materials. *J. Phys. Condens. Matter* **14**, 2745–2779 (2002).
44. J. P. Perdew, K. Burke, M. Ernzerhof, Generalized gradient approximation made simple. *Phys. Rev. Lett.* **77**, 3865–3868 (1996).
45. H. J. Monkhorst, J. D. Pack, Special points for Brillouin-zone integrations. *Phys. Rev. B* **13**, 5188 (1976).

Acknowledgments

Funding: This work was supported by the Air Force Office of Scientific Research (AFOSR) through grant no. FA9550-18-1-0072. L.S. acknowledges financial support from CNPq (grant no. 408525/2018-5) and high-performance computing facilities from LoboC/NACAD/UFRJ. This work was partly supported by the São Paulo State Foundation (FAPESP; grant nos. 2012/50259-8, 2015/11779-4 and 2017/01817-1), the Brazilian Nanocarbon Institute of Science and Technology (INCT/Nanocarbono), Conselho Nacional de Desenvolvimento Científico e Tecnológico (CNPq), and CAPES-PRINT (Programa Institucional de Internacionalização; grant no. 88887.310281/2018-00). This work has been funded by the Air Force Office of Scientific Research under award no. FA9550-18-1-0352. **Author contributions:** The manuscript was written through contributions of all the authors. H.L. and D.G. conducted the functionalization experiments and characterizations. D.G. and C.J.S.d.M. preformed the microabsorption measurements. L.S., C.M.M., and D.G. performed the first-principles calculations. A.D. and S.D. helped with device fabrication and tests. E.K. and R.B.N.B. synthesized the pristine MoS_2 materials. K.F., T.Z., and F.Z. helped with TEM characterization and simulation. Y.L., A.L.E., and Y.-T.Y. provided guidance and helped analyze the data. R.C.S. helped with XPS measurements and analysis. M.T., S.D., and C.J.S.d.M. supervised the whole work. All authors gave approval to the final version of the manuscript. **Competing interests:** The authors declare that they have no competing interests. **Data and materials availability:** All data needed to evaluate the conclusions in the paper are present in the paper and/or the Supplementary Materials. Additional data related to this paper may be requested from the authors.

Submitted 21 May 2020
Accepted 20 October 2020
Published 2 December 2020
10.1126/sciadv.abc9308

Citation: H. Liu, D. Grasseschi, A. Dodda, K. Fujisawa, D. Olson, E. Kahn, F. Zhang, T. Zhang, Y. Lei, R. B. N. Branco, A. L. Elías, R. C. Silva, Y.-T. Yeh, C. M. Maroneze, L. Seixas, P. Hopkins, S. Das, C. J. S. de Matos, M. Terrones, Spontaneous chemical functionalization via coordination of Au single atoms on monolayer MoS_2. *Sci. Adv.* **6**, eabc9308 (2020).

Science Advances

Spontaneous chemical functionalization via coordination of Au single atoms on monolayer MoS_2

He Liu, Daniel Grasseschi, Akhil Dodda, Kazunori Fujisawa, David Olson, Ethan Kahn, Fu Zhang, Tianyi Zhang, Yu Lei, Ricardo Braga Nogueira Branco, Ana Laura Elías, Rodolfo Cruz Silva, Yin-Ting Yeh, Camila M. Maroneze, Leandro Seixas, Patrick Hopkins, Saptarshi Das, Christiano J. S. de Matos and Mauricio Terrones

Sci Adv **6** (49), eabc9308.
DOI: 10.1126/sciadv.abc9308

Science Advances (ISSN 2375-2548) is published by the American Association for the Advancement of Science, 1200 New York Avenue NW, Washington, DC 20005. The title *Science Advances* is a registered trademark of AAAS.